

Geophysical Research Letters®



RESEARCH LETTER

10.1029/2022GL100351

Key Points:

- We use ocean bottom seismometer data to image elongated upper mantle *P*-wave velocity anomalies, of order $\pm 2\%$, striking parallel to free air gravity lineations
- These features extend >200 km deep, requiring thermal anomalies and small-fraction partial melts related to volatiles in the asthenosphere
- Anomalies are inferred to arise from small-scale convective cells beneath the plate with a planform parallel to absolute plate motion

Supporting Information:

Supporting Information may be found in the online version of this article.

Correspondence to:

Z. C. Eilon,
eilon@ucsb.edu

Citation:

Eilon, Z. C., Zhang, L., Gaherty, J. B., Forsyth, D. W., & Russell, J. B. (2022). Sub-lithospheric small-scale convection tomographically imaged beneath the Pacific plate. *Geophysical Research Letters*, 49, e2022GL100351. <https://doi.org/10.1029/2022GL100351>

Received 12 JUL 2022

Accepted 6 SEP 2022

Author Contributions:

Conceptualization: James B. Gaherty, Donald W. Forsyth

Data curation: Zachary C. Eilon, Lun Zhang, James B. Gaherty, Joshua B. Russell

Formal analysis: Zachary C. Eilon, Lun Zhang, Joshua B. Russell

Funding acquisition: Zachary C. Eilon, James B. Gaherty, Donald W. Forsyth

Investigation: Zachary C. Eilon, Lun Zhang, James B. Gaherty, Donald W. Forsyth, Joshua B. Russell

© 2022 The Authors.

This is an open access article under the terms of the [Creative Commons Attribution-NonCommercial License](#), which permits use, distribution and reproduction in any medium, provided the original work is properly cited and is not used for commercial purposes.

Sub-Lithospheric Small-Scale Convection Tomographically Imaged Beneath the Pacific Plate

Zachary C. Eilon¹ , Lun Zhang¹, James B. Gaherty² , Donald W. Forsyth³, and Joshua B. Russell³ 

¹University of California Santa Barbara, Santa Barbara, CA, USA, ²Northern Arizona University, Flagstaff, AZ, USA,

³Brown University, Providence, RI, USA

Abstract Small-scale convection beneath the oceanic plates has been invoked to explain off-axis nonplume volcanism, departure from simple seafloor depth-age relationships, and intraplate gravity lineations. We deployed 30 broadband ocean bottom seismometer stations on ~ 40 Ma Pacific seafloor in a region notable for gravity anomalies, measured by satellite altimetry, elongated parallel to plate motion. *P*-wave teleseismic tomography reveals alternating upper mantle velocity anomalies on the order of $\pm 2\%$, aligned with the gravity lineations. These features, which correspond to $\sim 300^\circ\text{--}500^\circ\text{K}$ lateral temperature contrast, and possible hydrous or carbonatitic partial melt, are—surprisingly—strongest between 150 and 260 km depth, indicating rapid vertical motions through a low-viscosity asthenospheric channel. Coherence and admittance analysis of gravity and topography using new multibeam bathymetry soundings substantiates the presence of mantle density variations, and forward modeling predicts gravity anomalies that qualitatively match observed lineations. This study provides observational support for small-scale convective rolls beneath the oceanic plates.

Plain Language Summary Covered by kilometers of water and therefore hard to access, Earth's oceanic tectonic plates have several features we cannot explain. Among these are linear undulations (“rolls”) in the strength of gravitational acceleration at the sea surface. Using data from a rare underwater seismic experiment, we have produced 3-D maps of seismic properties of the Earth's sub-surface in a location of clear gravity rolls. We find linear blobs of fast and slow material in the mantle beneath the oceanic plate, parallel to the gravity features. These represent cold sinking and warmer rising material, revealing a highly dynamic convective system underneath the plate, which has long been theorized but not previously directly observed at this scale.

1. Introduction

Traditional plate tectonic models fail to explain several aspects of the oceanic lithosphere. For instance, widespread off-axis, nonplume volcanism within the Pacific plate has an unknown origin (Ballmer et al., 2009; Sandwell et al., 1995), while the depth-age relationship predicted by lithospheric conductive cooling models breaks down in old (>70 Ma) ocean plates with anomalously shallow seafloor topography and high heat flow (Crosby et al., 2006; Parsons & McKenzie, 1978; Parsons & Sclater, 1977; Stein & Stein, 1992). Sub-lithospheric small-scale convection (SSC) (Ballmer et al., 2007; Buck, 1985; Haxby & Weissel, 1986) has been proposed to explain these phenomena. This dynamic process, which is favored by a thicker, lower-viscosity asthenospheric layer, would increase the heat flow at the base of the lithospheric thermal boundary layer and could concentrate upwelling and consequent melting. SSC spontaneously develops in the upper mantle due to the instabilities at the base of the lithosphere whenever its thickness exceeds a critical value (Ballmer et al., 2007; Buck & Parmentier, 1986). It is expected to take the form of convective rolls aligned with absolute plate motion (APM) (Buck & Parmentier, 1986; Richter & Parsons, 1975) (Figure 1b) due to shear between the plate and the deeper mantle. Despite the geodynamic significance of SSC beneath the oceanic plates, it has never previously been directly imaged at length scales $<\sim 2,000$ km (French et al., 2013) with seismic tomography beneath a mature oceanic plate.

To date, the most powerful argument for widespread SSC beneath the plates is free air gravity lineations observed in the oceans, aligned parallel to APM and with a wavelength of $\sim 150\text{--}400$ km, comparable to SSC predictions (Haxby & Weissel, 1986). Others have proposed alternative explanations for these gravity anomalies, including mechanical modification of the lithosphere and viscous fingering (Bull et al., 1992; Cormier et al., 2011; Gans et al., 2003; Sandwell & Fialko, 2004; Sandwell et al., 1995). Lithospheric boudinage (nonlinear lithospheric

Methodology: Zachary C. Eilon, Lun Zhang, Donald W. Forsyth
Resources: Zachary C. Eilon, James B. Gaherty
Software: Zachary C. Eilon
Supervision: Zachary C. Eilon, James B. Gaherty, Donald W. Forsyth
Validation: Zachary C. Eilon, Lun Zhang
Visualization: Zachary C. Eilon
Writing – original draft: Zachary C. Eilon, Lun Zhang
Writing – review & editing: Zachary C. Eilon, James B. Gaherty, Donald W. Forsyth, Joshua B. Russell

extension) or thermal contraction bending (Figure 1b) can produce elongated topographic and gravity undulations. Associated cracking might provide conduits for upward percolation of preexisting asthenospheric melt to form volcanic ridges; in this case, the drainage of melt might lead to shallow high-velocity anomalies beneath the ridges (Karato & Jung, 1998). Viscous fingering, caused by lateral intrusion of low-viscosity material within a thin asthenospheric channel (Figure 1b), has also been proposed to explain spreading-aligned ridge-adjacent seamounts, gravity variation, and long-wavelength velocity anomalies beneath young seafloor (Holmes et al., 2007; Weeraratne et al., 2007). Our study area is on older seafloor in a region with no volcanic ridges or major seamounts. Notably, gravity lineations here obliquely cross fracture zones (that record fossilized relative plate motion), suggesting they are not inherited from the mid-ocean ridges.

Discriminating the above hypotheses requires tomographic resolution of features with <200 km lateral wavelength in the upper mantle, together with high-precision local constraints on bathymetry. Sparse island stations and ocean basin-traversing seismic rays offer only coarse imaging of the oceanic upper mantle. A previous study, the GLIMPSE ocean bottom seismometer (OBS) experiment (Forsyth et al., 2006), aimed to probe gravity lineations in ~2–10 Ma Pacific plate just west of the East Pacific Rise. Body (Harmon et al., 2007) and Rayleigh wave (Weeraratne et al., 2007) imaging revealed elongate low-velocity lineaments beneath volcanic ridges with lateral wavelength of order ~250 km. Substantial data loss precluded fine depth resolution with body waves, but velocity variation was estimated using surface waves to reside at <70 km depth. No other OBS experiments before or since have imaged uppermost mantle 3-D isotropic wave speed variations suggestive of small-scale convection in regions unperturbed by plume or other intra- or inter-plate volcanic activity.

2. Data

The Pacific OBS Research into Convecting Asthenosphere (ORCA) experiment (Eilon et al., 2022) deployed 30 OBS instruments across a $500 \times 500 \text{ km}^2$ footprint on ~40 Ma lithosphere northeast of the Marquesas Islands. These instruments, deployed for 13 months, included three-component broadband seismometers and differential pressure gauges. The array was oriented approximately orthogonal to $\pm 15 \text{ mGal}$ free air gravity lineations observed from Seasat altimetry (Haxby & Weissel, 1986), with an aperture spanning 2–3 wavelengths (~500 km) of the gravity rolls (Figure 1a). This experiment also collected new high-resolution multibeam swath data, which has been integrated into the global seafloor database (Smith & Sandwell, 1997) to provide substantially better constrained bathymetry in this region.

We extracted the vertical seismic and pressure waveforms for *P*-wave arrivals recorded on the ORCA array from teleseismic events ($>30^\circ$ distance; Figure 1) in the Global Centroid Moment Tensor catalog between April 2018 and May 2019 with moment magnitudes ≥ 5.5 . For each event, we measured relative arrival times of direct *P*-waves using multichannel cross-correlation (MCCC; Figure S1 in Supporting Information S1) (VanDecar & Crosson, 1990) on vertical and pressure records independently, yielding 1,096 and 598 differential travel times, respectively. The vertical and pressure records were nominally filtered to 0.3–0.6 Hz and 0.4–2 Hz, respectively, with some manual adjustment to optimize the highest frequency signal preservation. We combined these data (see Supporting Information S1) to yield 1196 high-quality *P*-wave travel times (Figure S2a in Supporting Information S1).

3. Methods

We inverted these differential travel times for 3-D upper mantle *P*-wave velocity perturbations (δV_p) using finite frequency tomography. We regularized the inverse problem using model norm damping and first derivative damping (i.e., “flattening”) with a horizontal-to-vertical smoothing ratio of 2. Optimal regularization parameter values were determined by an L-test. We weighted observations by estimating travel time errors *a posteriori* during the MCCC process. To avoid unrealistically low estimated errors, we set a minimum standard deviation of 0.0625 s. We solved for station and event static terms. For a comprehensive description of the inverse problem, see the Supporting Information S1.

To explore apparent lineations in observed velocity structure, we conducted a series of “2.5-D” inversions by enforcing flattening (i.e., no model variation) along a single horizontal direction, seeking a lineation direction that minimized data misfit. We also evaluated the resolution and reliability of our inversion through input-output tests that included checkerboard structures (Figure S5 in Supporting Information S1) and velocity lineations that mimic features of dynamical interest (Figure S4 in Supporting Information S1). For checkerboard tests, we quantify feature recovery using semblance (Zelt, 1998) computed at each point over a 3-D volume with a radius equal

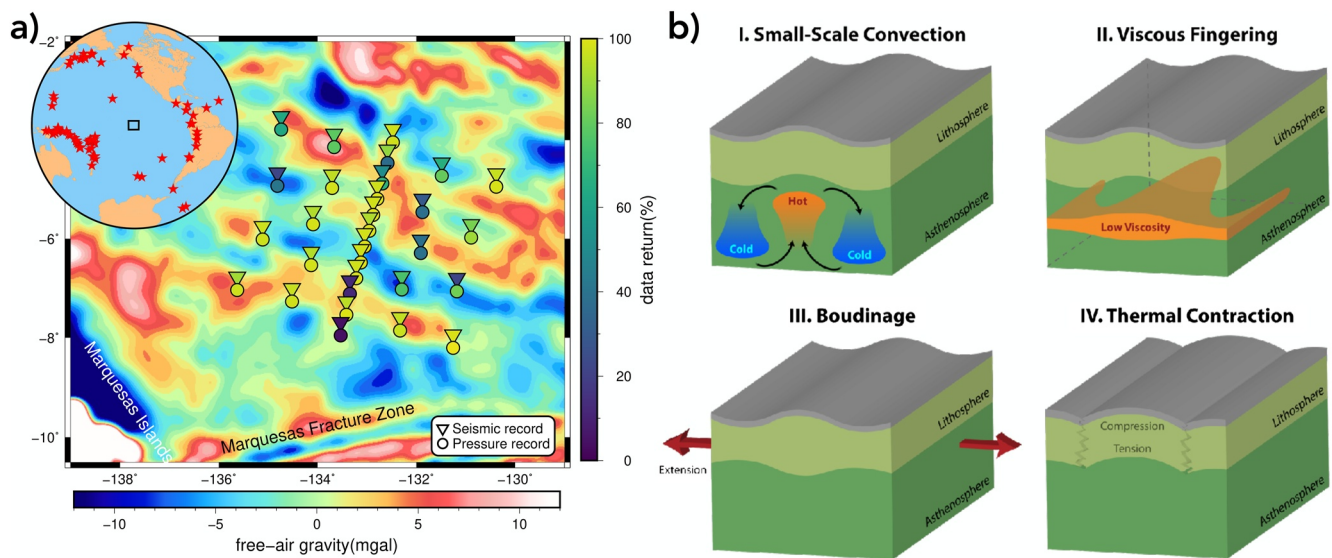


Figure 1. Map of the research area (a) and schematics of candidate processes causing gravity lineations (b). (a) Broadband OBS array comprising three-component seismometers (triangles) with differential pressure gauge (circles). Symbol colors indicate fractional data return, and the underlying map shows filtered free air gravity anomalies (Figure S9 in Supporting Information S1). Inset shows the location of the array, with stars representing earthquakes from which differential travel times were measured. (b) Block diagrams showing exaggerated lithospheric and asthenospheric structures proposed to explain free air gravity undulations (adapted after Weeraratne et al., 2007). Any bathymetric anomalies, exaggerated here, are highly contingent on the elastic thickness of the lithosphere.

to the checker length scale. Finally, we performed a suite of inversions for which the model nodes below and above various “squeezing depths” were heavily damped. By evaluating the fractional reduction in overall data fit for each squeezed case and observing whether or not the inversion reinjects structure once the damping is relaxed (see Supporting Information S1), we determined the depth range over which the data required major velocity anomalies.

4. Results

4.1. Tomographic Inversion

Simple thermal cooling models predict essentially no upper mantle velocity heterogeneity on the length scale of this array. Nonetheless, we measured differential arrival times of up to ± 0.5 s (with an root mean squared (RMS) value of 0.27 s). This travel time variance substantially exceeds signal that can be produced in the crust, and systematic back azimuthal variations seen at several stations confirm this signal to have an upper mantle origin (Figure S2 in Supporting Information S1).

Our 3D tomographic model shows prominent alternating velocity anomaly bands in the upper mantle, parallel to local gravity lineations, with lateral wavelengths ~ 250 – 300 km (Figure 2). The amplitude of these anomalies is on the order of $\pm 2\%$ ($\pm 2.3\%$ for the 1–99 percentiles, or $\pm 1.8\%$ for the 2.5–97.5 percentiles, in the best resolved regions; Figure S8 in Supporting Information S1). The final RMS data error was 0.23 s, the RMS of event static values was 0.10 s and the RMS of station static values was 0.02 s. The weighted variance reduction was 85%, indicating good data fit.

4.2. Testing the Model

To test for preferred lineations of anomalies, we performed a 2.5-D inversion. By grid searching through possible smoothing directions, we showed (Figure 3 and Figure S7 in Supporting Information S1) that best fit to data (78% as good as the full 3-D model) involves structure elongated in the 115° direction (Figure 3b). We infer that this direction reflects the dominant structural elongation. This orientation is subparallel to (independently constrained) gravity lineations and local APM. Note that this minimum misfit 2.5-D model (Figure 3b) was used to compute 1-D gravity variations (Figure 4).

Synthetic tests indicated that our data coverage can indeed recover the geometry and position of the observed features (Figure 3, Figures S4 and S5 in Supporting Information S1). These tests—especially at the model

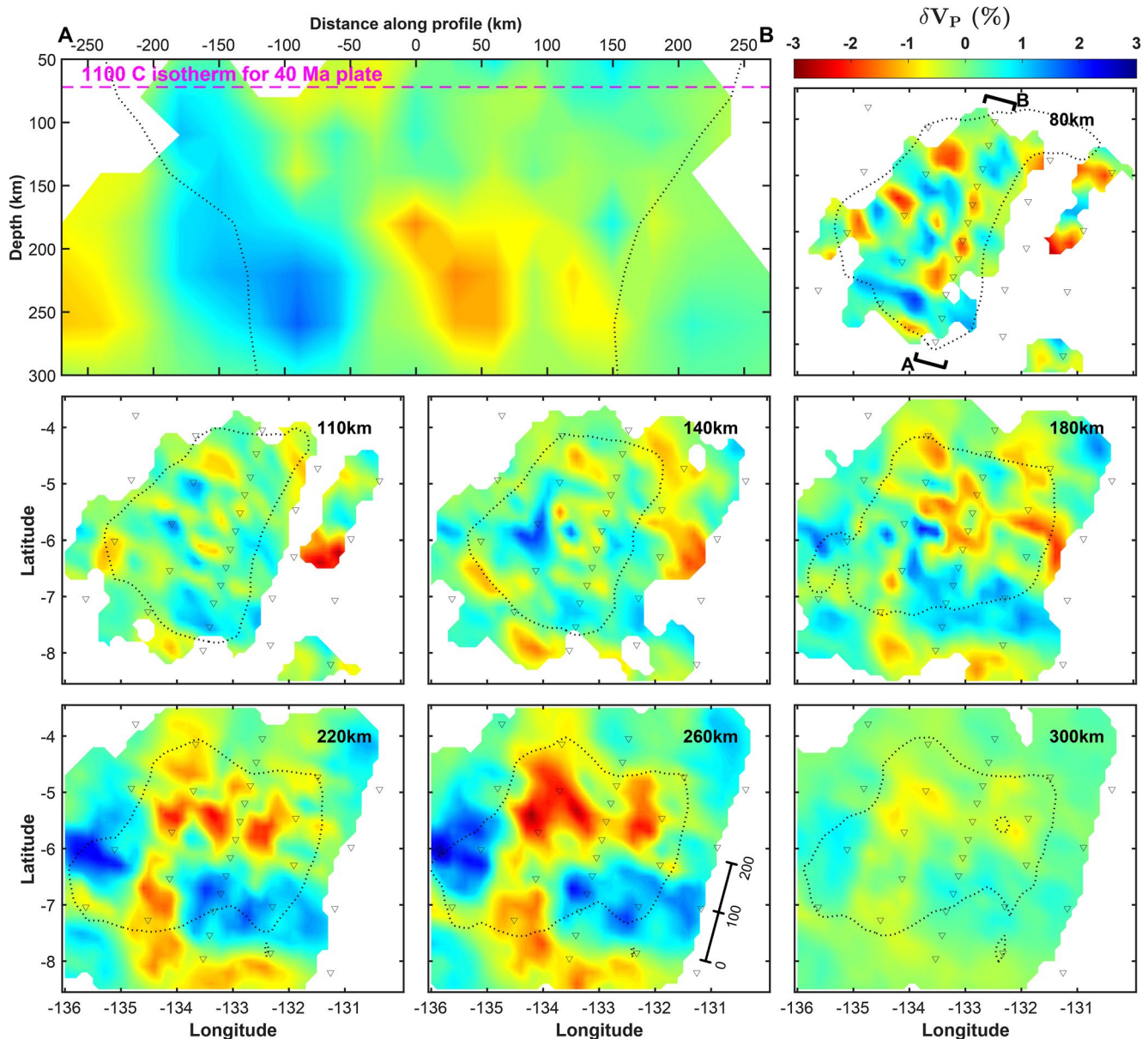


Figure 2. The tomographic model. A vertical slice (top left) and several horizontal slices through our preferred 3-D δV_P model, where structure is shown only for model nodes with “hit quality” (Eilon et al., 2015) above 0.3. Black-dotted line shows regions with a semblance greater than 0.7. Scale bar values are in km. The vertical section depicts values averaged ± 30 km in the direction perpendicular to the line of the section (indicated by black brackets in the 80 km depth cross-section), to avoid overly emphasizing any particular plane.

edges—suffer from as much as 40% amplitude loss due to sparse seismic ray coverage. This observation, typical for these sorts of regularized inversions, theoretically implies that observed velocity, and hence inferred temperature, contrasts are in fact lower bounds.

We individually tested shallow squeezing and deep squeezing, finding that the data require relatively deep anomalies: at least 140 km, and as much as 300 km in depth (Figure S4 and S6 in Supporting Information S1). We attempted to quantitatively determine the optimal depth range for the most prominent mantle velocity anomalies by squeezing structure into a moving window of three model layers (Figure 3). These tests showed that the data required the most prominent anomalies to be fit by structure within the 180–260 km depth range. This finding is not particular to a three-layer test; similar two- and four-layer tests confirmed that the 140–260 km depths are most important to fitting the data. This finding does not preclude structure at other depths in the model, rather it indicates that velocity anomalies in this depth range have the greatest influence on measured travel times.

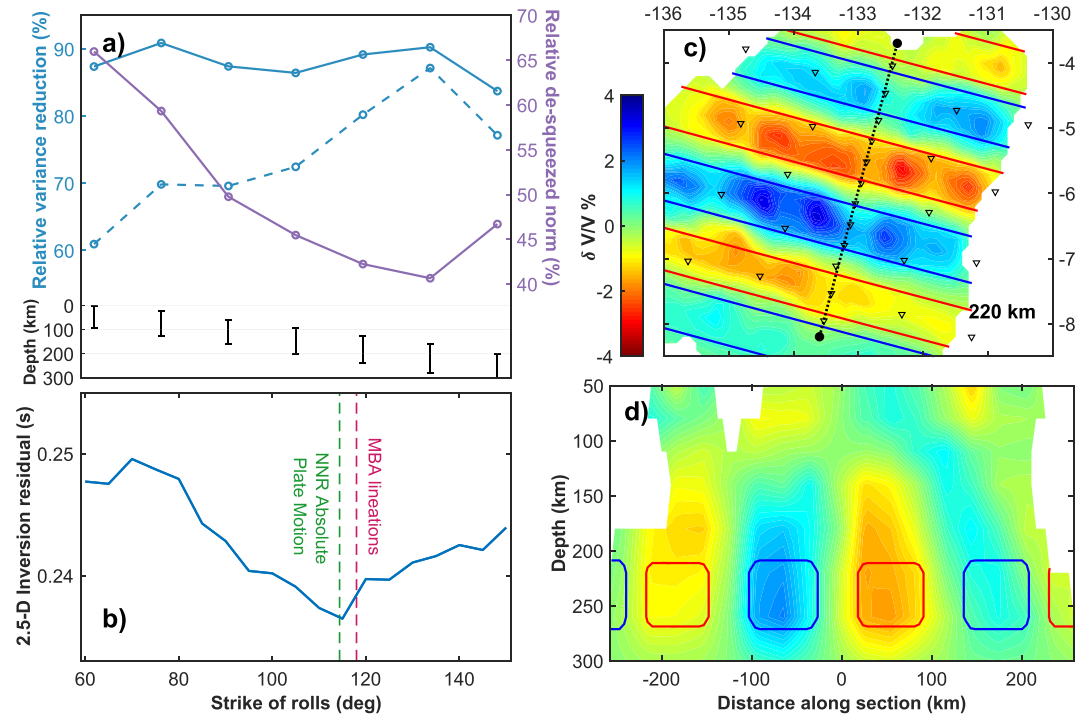


Figure 3. Tests of the tomographic model. (a) Squeezing tests of anomaly depth. Lower subplot shows depth extent over which structure was allowed to enter into the model space. Upper subplot shows data fit (solid and dashed blue lines show weighted and unweighted variance reduction, respectively, and higher values indicate better data fit) and explanatory power of the unsqueezed region of model space (purple line; low values indicate the squeezed model does a better job of explaining the data) for the associated models. Variance reduction is plotted relative to (i.e., normalized by) the undamped, preferred, model. De-squeezed model norm is plotted relative to the norm of the squeezed model in each iteration and can thus be thought of as fractional model addition once squeezing is relaxed. (b) Grid search tests of feature elongation direction, showing data misfit (residual) of a 2.5-D model varying with orientation. (c) Horizontal slice and (d) vertical section through models yielded by synthetic recovery tests with input rectangular velocity anomalies (dashed lines) of $\pm 4\%$.

Lastly, we explored the depth extent of imaged features by increasing the model base to 480 km (Figure S6 in Supporting Information S1). We found that although some structure is smeared to depths >300 km, the pattern of the anomalies is extremely similar to the preferred model, and the strongest anomalies are still present in the 150–300 km depth range.

4.3. Gravity Signals

The ORCA experiment measured high-resolution multibeam bathymetry throughout the OBS array footprint, allowing for detailed comparison with gravity (Figure S9 in Supporting Information S1). To identify subsurface density heterogeneity, we computed free air coherence and admittance, and the theoretical mantle Bouguer anomaly (MBA; see in Supporting Information S1). Coherence refers to the similarity (in the wavenumber domain) between gravity and bathymetry signals, and admittance refers to the ratio of power in the gravity field to that in the bathymetry field. Taken together, these can reveal the degree of isostatic compensation versus flexural support of topographic loads and the depth or wavelength of (sub) surface density anomalies (e.g., Forsyth, 1985). At wavelengths greater than 20 km, observed free air admittance in this region is approximately 0.025 mGal/m. This value is substantially less than the theoretical admittance for uncompensated topography, but also significantly greater than the prediction for topography compensated at the Moho (Figure S10 in Supporting Information S1).

5. Discussion and Conclusions

5.1. Thermal Anomalies

The tomographic models show alternating slow and fast δV_p features within the oceanic asthenosphere. We infer that these features result from hot upwellings and cold downwellings, respectively. These cells take the

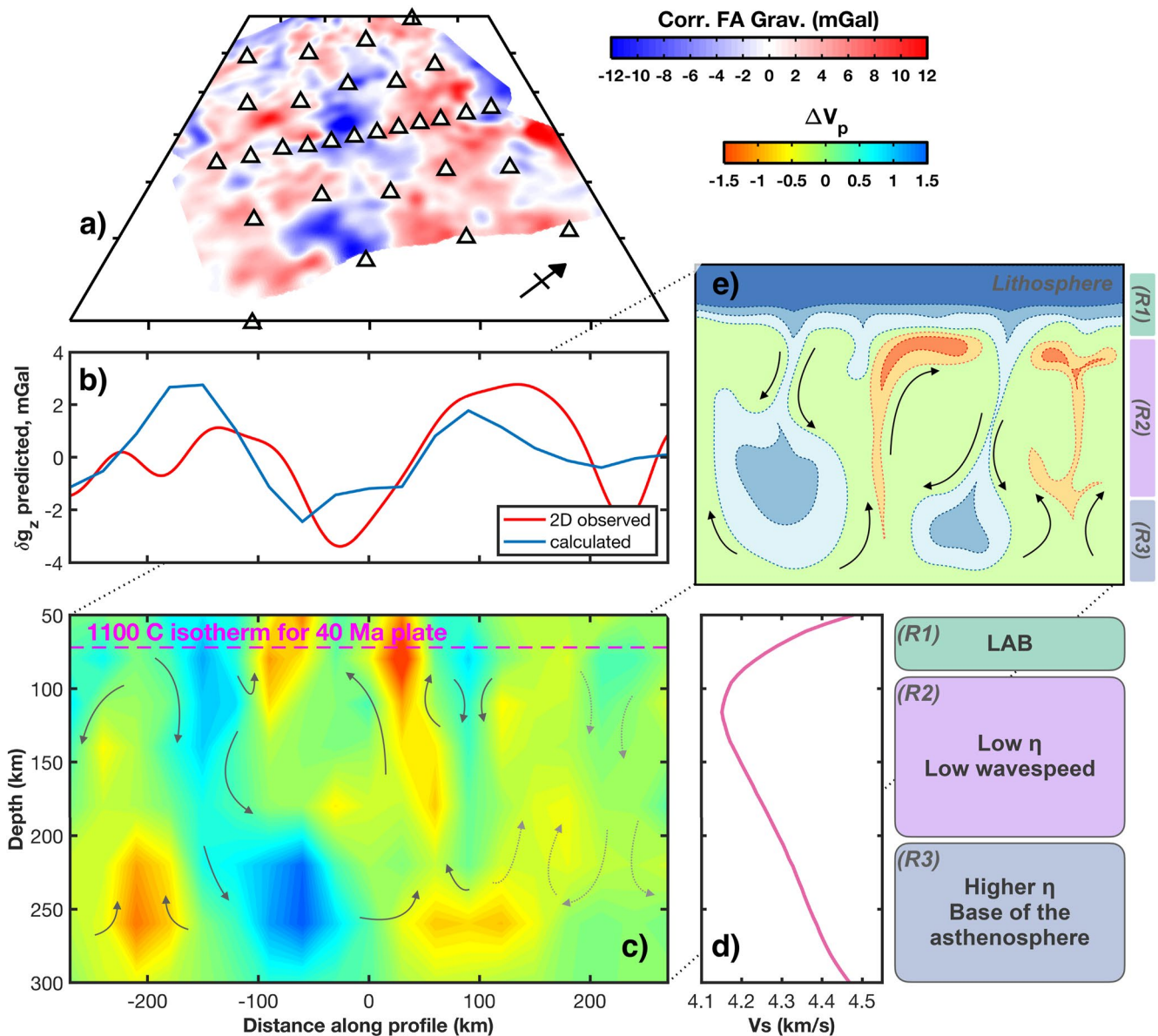


Figure 4. Dynamic summary and comparison between gravity and tomography. (a) Perspective view of the mantle Bouguer gravity anomaly corrected for effects of bathymetry and filtered from 600 to 10 km (see Figure S9 in Supporting Information S1). (b) One-dimensional variation in gravity anomaly obtained from sinusoidal fitting of the observed field (red) and velocity-temperature-density forward modeling (blue) of the model depicted in panel (c). The orientation of the section is 030° , roughly perpendicular to the gravity lineations. (c) Cross-section through a 2.5-D velocity model, perpendicular to enforced smoothing direction. Arrows help guide the eye for interpretive purposes; they do not reflect mantle flow modeling. (d) 1-D shear velocity profile obtained from inversion of Rayleigh wave phase velocities averaged across the ORCA array (Russell, 2021). At right are interpretive rheological regimes (R1-3) described in the main text. η is viscosity; LAB is the Lithosphere-Asthenosphere Boundary. (e) Illustrative cartoon cross-section of small-scale convection beneath the plate. Bluer colors correspond to colder, denser material, and redder colors correspond to hotter and less dense material.

approximate form of cylindrical rolls, with horizontal length scale $\sim 250\text{--}300$ km and aspect ratios of approximately unity. These features are not consistent with lithospheric warping (boudinage or cracking), which predicts negligible, and certainly not >200 km deep, upper-mantle velocity variations. They are also not consistent with viscous fingering, which would require velocity variations confined to a shallow (<100 km deep) and thin (<30 km thick) channel (Weeraratne and Parmentier, pers. comm.) Rather, these observations provide the first tomographic evidence for small-length-scale thermal convection beneath the oceanic plates, aligned by shear between the plate and underlying deeper mantle.

Differential travel time tomography constrains lateral velocity gradients, not absolute velocities. The $\sim 4\%$ peak-to-peak amplitude of the observed velocity anomalies is relatively high. Absent melt, it implies up to $\sim 500^\circ\text{C}$ lateral temperature variations (see Figure S8 in Supporting Information S1). Our default expectation is that SSC is driven here by positive density anomalies that drip or sink from the base of the lithospheric thermal boundary layer. In this framework, the fast dV_p anomalies correspond to material that is cold in an absolute sense, while the slow dV_p anomalies represent relatively warm ambient mantle.

However, upwelling parcels displaced by the downwellings must undergo adiabatic decompression. If the mantle contains dissolved volatiles, this upwelling material could produce small-fraction hydrous and/or carbonatitic melt fractions even at depths up to 200 km (Dasgupta et al., 2013; Hirschmann, 2010). Melting could introduce a small active component to upwelling by reducing density and viscosity. Melt would also lower the absolute P -wave velocity in the upwelling cells. Accounting for both elastic and anelastic effects (see Supporting Information S1), the observed peak-to-peak dV_p variation can also be explained by a 0.5% melt fraction, together with a dT of $\sim 300^\circ\text{C}$ (Figure S8 in Supporting Information S1). We prefer this latter (temperature plus melt) scenario for explaining observed anomalies, since the implied temperature gradient is more consistent with (although still greater than) the temperature contrast invoked in numerical models of sub-lithospheric SSC (Ballmer et al., 2009; Manjón-Cabeza Córdoba & Ballmer, 2021). This same analysis predicts a Q_μ of 100–180 in the oceanic asthenosphere, consistent with previous observations (Ma et al., 2020).

5.2. Gravity Analysis and Modeling

Gravity anomalies here provide further insight. Free air admittance indicates some degree of isostatic compensation. The remaining support for bathymetry must come from plate strength, in line with previous >15 km estimates of effective elastic thickness here (Fischer et al., 1986). Compensation must result from some combination of crustal thickness variations and upper mantle density anomalies, and three primary observations suggest substantial influence from the upper mantle. First, MBA anomalies here (striking $\sim 120^\circ$) are oriented subparallel to plate motion ($\sim 115^\circ$), rather than the paleo-spreading direction inferred from abyssal hill fabric and nearby fracture zones ($\sim 75^\circ$, although we do note a due E-W swath of seafloor in this region with $\sim 105^\circ$ apparent spreading direction indicated by the trend of the abyssal hill topography (Eilon et al., 2022), perhaps due to oblique spreading, a ridge jump or large overlapping spreading center). Second, if observed gravity and bathymetry anomalies were created from a single mechanism then the coherence should be unity. Instead, we observe coherence lower than 0.7 associated with the longest wavelengths (Figure S10 in Supporting Information S1). Finally, the predicted free air anomaly for compensation at Moho depths underpredicts the admittance, requiring either deeper compensation or density anomalies beneath an elastic plate with flexural rigidity that dampens the topographic expression. Our inference is that multiple mechanisms are at play here, pointing to the loading of a finite-rigidity plate from below as a result of density variations in the mantle, in addition to “frozen-in” partial compensation of the topographic relief by variations in crustal thickness.

As a proof of concept, we explored the correspondence between the MBA and our velocity model. For simplicity, and given the strongly linear features in both models, we collapsed the MBA to 1.5 dimensions (i.e., varying in the roll-perpendicular-direction but homogenous in the roll-parallel-direction), using a log-spaced sinusoidal basis. The best fit 1.5-D gravity field (explaining 28% of the full 2-D signal) comprises lineations aligned 118° from north. We compare this gravity anomaly to the (minimum-misfit) 2.5-D velocity model smoothed along 115° . We consider dV_p variations only in the plane defined by the vertical and the direction perpendicular to the gravity rolls (Figure 4). There is no direct association between the pattern of deep (200–300 km) dV_p anomalies and the residual gravity other than similarity in their wavelength (225–300 km) and the orientation of the lineations. This is unsurprising: periodic density anomalies at depth approximately equal to their wavelength should negligibly affect surface gravity due to upward continuation. However, using our 2.5-D tomography model to forward calculate 1.5-D gravity variations (see Supporting Information S1, and note this calculation used the more modest temperature variation outlined above, adding support to that scenario), we found a good qualitative match between the observed and predicted signal, where the predicted signal is dominated by the shallowest features in the velocity model (Figure 4). Although this portion of the model is not as well resolved, the agreement is striking and demonstrates that mantle temperature heterogeneity alone can theoretically explain the MBA gravity anomaly.

5.3. Asthenospheric Rheology

The depth, vertical extent, and wavelength of putative convective features imaged in this study connect to the rheology of the asthenosphere. The presumed source of convective instability is near the base of the plate. For 40 Ma oceans (assuming mantle potential temperature, T_m , of 1,350°C and thermal diffusivity of 10^{-6} m²/s), the depth to the 1,150°C isotherm (the $0.85 T_m$ value often used to approximate the thermal lithosphere-asthenosphere boundary (LAB)) is 73 km. The agreement between the strike of the rolls and local APM in a no-net rotation reference frame (DeMets et al., 2010), together with the lack of another obvious alternative source for small-scale lateral thermal gradients, argues that these features are not deep-rooted but derive from convective processes near the bottom of the plate. Station spacing limits our resolution shallower than ~50 km, but synthetic recovery tests indicate that we should have imaged large-scale velocity anomalies in the 100–200 km depth range, if they were present (Figures S4 and S5 in Supporting Information S1). It is surprising, then, that the strongest velocity features in the model are as deep as 250 km and that squeezing tests suggest that the strongest anomalies are deeper than 200 km (Figure 3).

Rayleigh wave imaging at young ORCA (40 Ma) versus NoMelt (70 Ma crust) indicates that the young ORCA region exhibits anomalously slow absolute shear velocity beneath the plate (Figure 4), with a broad velocity minimum from 75 to 200 km depth (Russell et al., 2021). Small-scale convection is favored by a thicker low-viscosity layer, and the middle of this layer is expected to be roughly isothermal. Our observed anomalies appear deeper than the slowest (and presumably weakest) part of the asthenosphere. It is possible that density anomalies are preserved at lithospheric levels (<100 km depth) and deeper than 200 km due to higher viscosity, while the lowest-viscosity central asthenosphere is roughly isothermal, perhaps containing convective structures too fine to be resolved by our data (as illustrated by a synthetic test; Figure S11 in Supporting Information S1). A similar mechanism has been suggested to explain a mid-asthenosphere minimum in the strength of azimuthal anisotropy observed by other focused OBS arrays (Lin et al., 2016; Russell et al., 2019).

This suite of observations suggests a sub-lithospheric SSC system wherein gravity and velocity anomalies correspond to the upper and lower thermal boundary layers of an asthenosphere-scale convective system, respectively. We posit three depth regimes (Figure 4). R1: The base of the plate (50–100 km), the source of the density instabilities, and part of the Bouguer gravity anomalies. The elastic lithosphere partially damps the effect on bathymetry. R2: The low-viscosity center of the asthenosphere (100–200 km), coinciding with the lowest velocities in a surface-wave-derived 1-D shear velocity model (Figure 4). Body-wave-imaged anomalies in this regime are minimal, despite good resolving power. We infer that once an instability develops, it sinks rapidly through the low-viscosity asthenosphere (Ballmer et al., 2009), perhaps leaving behind thin convective sheets or spokes connecting regimes R1 and R3 that are too narrow to be imaged tomographically (Figure S11 in Supporting Information S1). R3: A higher viscosity base of the asthenosphere (200–300 km), where high-density anomalies encounter resistance to sinking and pile up, making for clearly imaged velocity anomalies. Ambient mantle displaced upwards at this depth begins to melt (requiring volatiles to reduce the solidus (Dasgupta et al., 2013; Hirschmann, 2010)), reducing seismic velocities in the upwelling volumes between the downwelling limbs.

This work provides evidence for a highly dynamic asthenospheric system beneath the central oceanic plates, involving small-scale lithospheric delamination, and small-fraction hydrous and/or carbonatite melt. Since intraplate volcanism is not ubiquitous in the oceans, upward pathways for melt transport through the lithosphere must be rare. Rather, this melt may pond or freeze in laminae at the base of the plate, contributing to the sharp and possibly radially anisotropic LAB structure observed widely in the Pacific (Beghein et al., 2014; Kawakatsu et al., 2009; Stern et al., 2015). In addition, SSC might introduce uneven topography on the LAB that is not a simple function of age. Together, these phenomena help explain the variability in seismic discontinuities in the uppermost (<100 km depth) oceanic mantle (Schmerr, 2012; Tharimena et al., 2017).

Conflict of Interest

The authors declare no conflicts of interest relevant to this study.

Data Availability Statement

The seismic data from this experiment are available through the Incorporated Research Institutions for Seismology's Data Management Center, under the network code XE (2018–2019). Metadata information is catalogued within Eilon et al. (2022) (<https://doi.org/10.1785/0220210173>). Multibeam swath bathymetry data are available

via the Rolling Deck to Repository portal (<https://doi.org/10.7284/907958> and <https://doi.org/10.7284/908257>). Free air gravity data are available courtesy of the Satellite Geodesy research group at the Scripps Institution of Oceanography at https://topex.ucsd.edu/pub/global_grav_1min/ and bathymetry at https://topex.ucsd.edu/pub/global_topo_1min. Codes for all the analysis and figures above are provided via a Dryad repository (<https://doi.org/10.25349/D9R89J>) and the filtered gravity data are available at Zenodo (<https://doi.org/10.5281/zenodo.7038677>).

Acknowledgments

This work was funded by NSF grants OCE-1658491, OCE-1658214, OCE-1658070, and OCE-2051265. The OBS instruments were provided by the Scripps Institution of Oceanography, coordinated by the OBS Instrument Centre at the Woods Hole Oceanographic Institute. The authors are grateful to Dave Sandwell for sharing codes and illuminating discussions. The authors thank the ships' captains, crew, and research technicians, as well as the cruise science parties, who were all indispensable to collecting these data. The authors appreciate the helpful reviews by Emilie Hooft and Lindsay Worthington.

References

- Ballmer, M. D., Hunen, J. V., Ito, G., Bianco, T. A., & Tackley, P. J. (2009). Intraplate volcanism with complex age-distance patterns: A case for small-scale sublithospheric convection. *Geochemistry, Geophysics, Geosystems*, 10(6). <https://doi.org/10.1029/2009gc002386>
- Ballmer, M. D., Hunen, J. V., Ito, G., Tackley, P. J., & Bianco, T. A. (2007). Non-hotspot volcano chains originating from small-scale sublithospheric convection. *Geophysical Research Letters*, 34(23), L23310. <https://doi.org/10.1029/2007gl031636/pdf>
- Beghein, C., Yuan, K., Schmerr, N., & Xing, Z. (2014). Changes in seismic anisotropy shed light on the nature of the Gutenberg discontinuity. *Science*, 343(6176), 1237–1240. <https://doi.org/10.1126/science.1246724>
- Buck, W. R. (1985). When does small-scale convection begin beneath oceanic lithosphere? *Nature*, 313(6005), 775–777. <https://doi.org/10.1038/313775a0>
- Buck, W. R., & Parmentier, E. M. (1986). Convection beneath young oceanic lithosphere: Implications for thermal structure and gravity. *Journal of Geophysical Research: Solid Earth and Planets*, 91(B2), 1961–1974. <https://doi.org/10.1029/jb091ib02p01961>
- Bull, J. M., Martinod, J., & Davy, P. (1992). Buckling of the oceanic lithosphere from geophysical data and experiments. *Tectonics*, 11(3), 537–548. <https://doi.org/10.1029/91TC02908>
- Cormier, M.-H., Gans, K. D., & Wilson, D. S. (2011). Gravity lineaments of the Cocos Plate: Evidence for a thermal contraction crack origin. *Geochemistry, Geophysics, Geosystems*, 12(7). <https://doi.org/10.1029/2011gc003573>
- Crosby, A. G., McKenzie, D., & Sclater, J. G. (2006). The relationship between depth, age and gravity in the oceans. *Geophysical Journal International*, 166(2), 553–573. <https://doi.org/10.1111/j.1365-246x.2006.03015.x>
- Dasgupta, R., Mallik, A., Tsuno, K., Withers, A. C., Hirth, G., & Hirschmann, M. M. (2013). Carbon-dioxide-rich silicate melt in the Earth's upper mantle. *Nature*, 493(7431), 211–215. <https://doi.org/10.1038/nature11731>
- DeMets, C., Gordon, R. G., & Argus, D. F. (2010). Geologically current plate motions. *Geophysical Journal*, 181, 1–80. <https://doi.org/10.1111/j.1365-246x.2009.04491.x>
- Eilon, Z., Abers, G. A., Gaherty, J. B., & Jin, G. (2015). Imaging continental breakup using teleseismic body waves: The Woodlark Rift, Papua New Guinea. *Geochemistry, Geophysics, Geosystems*, 16(8), 2529–2548. <https://doi.org/10.1002/2015GC005835>
- Eilon, Z. C., Gaherty, J. B., Zhang, L., Russell, J., McPeak, S., Phillips, J., et al. (2022). The Pacific OBS research into convecting asthenosphere (ORCA) experiment. *Seismological Research Letters*, 93(1), 477–493. <https://doi.org/10.1785/0220210173>
- Fischer, K. M., McNutt, M. K., & Shure, L. (1986). Thermal and mechanical constraints on the lithosphere beneath the Marquesas swell. *Nature*, 322(6081), 733–736. <https://doi.org/10.1038/322733a0>
- Forsyth, D. W. (1985). Subsurface loading and estimates of the flexural rigidity of continental lithosphere. *Journal of Geophysical Research*, 90(B14), 12623–12632. <https://doi.org/10.1029/jb090ib14p12623>
- Forsyth, D. W., Harmon, N., Scheirer, D. S., & Duncan, R. A. (2006). Distribution of recent volcanism and the morphology of seamounts and ridges in the GLIMPSE study area: Implications for the lithospheric cracking hypothesis for the origin of intraplate, non-hot spot volcanic chains. *Journal of Geophysical Research*, 111(B11). <https://doi.org/10.1029/2005jb004075>
- French, S., Lekic, V., Romanowicz, B., Shekhawat, A., Alemi, A. A., McEuen, P. L., et al. (2013). Waveform tomography reveals channeled flow at the base of the oceanic asthenosphere. *Science*, 342(6155), 224–227. <https://doi.org/10.1126/science.1242248>
- Gans, K. D., Wilson, D. S., & Macdonald, K. C. (2003). Pacific plate gravity lineaments: Diffuse extension or thermal contraction? *Geochemistry, Geophysics, Geosystems*, 4(9), 1074. <https://doi.org/10.1029/2002GC000465>
- Harmon, N., Forsyth, D. W., Lamm, R., & Webb, S. C. (2007). P and S wave delays beneath intraplate volcanic ridges and gravity lineations near the East Pacific Rise. *Journal of Geophysical Research: Solid Earth and Planets*, 112(B3), 1961–2012. <https://doi.org/10.1029/2006jb004392>
- Haxby, W. F., & Weissel, J. K. (1986). Evidence for small-scale mantle convection from Seasat altimeter data. *Journal of Geophysical Research*, 91(B3), 3507–3520. <https://doi.org/10.1029/jb091ib03p03507>
- Hirschmann, M. M. (2010). Partial melt in the oceanic low velocity zone. *Physics of the Earth and Planetary Interiors*, 179(1–2), 60–71. <https://doi.org/10.1016/j.pepi.2009.12.003>
- Holmes, R. C., Webb, S. C., & Forsyth, D. W. (2007). Crustal structure beneath the gravity lineations in the Gravity Lineations, Intraplate Melting, Petrologic and Seismic Expedition (GLIMPSE) study area from seismic refraction data. *Journal of Geophysical Research*, 112(B7), B07316. <https://doi.org/10.1029/2006JB004685>
- Karato, S., & Jung, H. (1998). Water, partial melting and the origin of the seismic low velocity and high attenuation zone in the upper mantle. *Earth and Planetary Science Letters*, 157(3–4), 193–207. [https://doi.org/10.1016/s0012-821x\(98\)00034-x](https://doi.org/10.1016/s0012-821x(98)00034-x)
- Kawakatsu, H., Kumar, P., Takei, Y., Shinohara, M., Kanazawa, T., Araki, E., & Suyehiro, K. (2009). Seismic evidence for sharp lithosphere-asthenosphere boundaries of oceanic plates. *Science*, 324(5926), 499–502. <https://doi.org/10.1126/science.1169499>
- Lin, P., Gaherty, J. B., Jin, G., Collins, J. A., Lizarralde, D., Evans, R. L., & Hirth, G. (2016). High-resolution seismic constraints on flow dynamics in the oceanic asthenosphere. *Nature*, 535(7613), 438–541. <https://doi.org/10.1038/nature18012>
- Ma, Z., Dalton, C. A., Russell, J. B., Gaherty, J. B., Hirth, G., & Forsyth, D. W. (2020). Shear attenuation and anelastic mechanisms in the central Pacific upper mantle. *Earth and Planetary Science Letters*, 536, 116148. <https://doi.org/10.1016/j.epsl.2020.116148>
- Manjón-Cabeza Córdoba, A., & Ballmer, M. D. (2021). The role of edge-driven convection in the generation of volcanism – Part 1: A 2D systematic study. *Solid Earth*, 12(3), 613–632. <https://doi.org/10.5194/se-12-613-2021>
- Parsons, B., & McKenzie, D. (1978). Mantle convection and the thermal structure of the plates. *Journal of Geophysical Research*, 83(B9), 4485. <https://doi.org/10.1029/JB083iB09p04485>
- Parsons, B., & Sclater, J. G. (1977). An analysis of the variation of ocean floor bathymetry and heat flow with age. *Journal of Geophysical Research*, 82(5), 803–827. <https://doi.org/10.1029/jb082i005p0803>
- Richter, F. M., & Parsons, B. (1975). On the interaction of two scales of convection in the mantle. *Journal of Geophysical Research*, 80(17), 2529–2541. <https://doi.org/10.1029/jb080i017p02529/pdf>
- Russell, J., Gaherty, J. B., Eilon, Z. C., Forsyth, D. W., & Ekström, G. (2021). Heterogeneous mantle flow and deviations from half-space cooling observed beneath the central Pacific. In *AGU fall meeting 2021*. DI15C-0033.

- Russell, J. B. (2021). Structure and evolution of the oceanic lithosphere-asthenosphere system from high-resolution surface-wave imaging (PhD Thesis). *ProQuest Dissertations and Theses*. Retrieved from <https://www.proquest.com/dissertations-theses/structure-evolution-oceanic-lithosphere/docview/2492599842/se-2?accountid=14522>
- Russell, J. B., Gaherty, J. B., Lin, P.-Y. P., Lizarralde, D., Collins, J. A., Hirth, G., & Evans, R. L. (2019). High-resolution constraints on Pacific upper mantle Petrofabric inferred from surface-wave anisotropy. *Journal of Geophysical Research*, 35(3), 415–427. <https://doi.org/10.1029/2018jb016598>
- Sandwell, D., & Fialko, Y. (2004). Warping and cracking of the Pacific plate by thermal contraction. *Journal of Geophysical Research*, 109(B10). <https://doi.org/10.1029/2004jb003091>
- Sandwell, D. T., Winterer, E. L., Mammertick, J., Duncan, R. A., Lynch, M. A., Levitt, D. A., & Johnson, C. L. (1995). Evidence for diffuse extension of the Pacific plate from Pukapuka ridges and cross-grain gravity lineations. *Journal of Geophysical Research*, 100(B8), 15087–15099. <https://doi.org/10.1029/95JB00156>
- Schmerr, N. (2012). The gutenbergs discontinuity: Melt at the lithosphere-asthenosphere boundary. *Science*, 335(6075), 1480–1483. <https://doi.org/10.1126/science.1215433>
- Smith, W. H. F., & Sandwell, D. T. (1997). Global Sea floor topography from satellite altimetry and ship depth soundings. *Science*, 277(5334), 1956–1962. <https://doi.org/10.1126/science.277.5334.1956>
- Stein, C. A., & Stein, S. (1992). A model for the global variation in oceanic depth and heat flow with lithospheric age. *Nature*, 359(6391), 123–129. <https://doi.org/10.1038/359123a0>
- Stern, T. A., Henrys, S. A., Okaya, D., Louie, J. N., Savage, M. K., Lamb, S., et al. (2015). A seismic reflection image for the base of a tectonic plate. *Nature*, 518(7537), 85–88. <https://doi.org/10.1038/nature14146>
- Tharimena, S., Rychert, C., Harmon, N., & White, P. (2017). Imaging Pacific lithosphere seismic discontinuities—Insights from SS precursor modeling. *Journal of Geophysical Research: Solid Earth*, 122(3), 2131–2152. <https://doi.org/10.1002/2016JB013526>
- VanDecar, J. C., & Crosson, R. S. (1990). Determination of teleseismic relative phase arrival times using multi-channel cross-correlation and least squares. *Bulletin of the Seismological Society of America*, 80(1), 150–169.
- Weeraratne, D. S., Forsyth, D. W., Yang, Y., & Webb, S. C. (2007). Rayleigh wave tomography beneath intraplate volcanic ridges in the South Pacific. *Journal of Geophysical Research: Solid Earth and Planets*, 112(B6), B06303. <https://doi.org/10.1029/2006jb004403>
- Zelt, C. A. (1998). Lateral velocity resolution from three-dimensional seismic refraction data. *Geophysical Journal International*, 135(3), 1101–1112. <https://doi.org/10.1046/j.1365-246x.1998.00695.x>

References From the Supporting Information

- Abers, G. A., & Hacker, B. R. (2016). A MATLAB toolbox and Excel workbook for calculating the densities, seismic wave speeds, and major element composition of minerals and rocks at pressure and temperature. *Geochemistry, Geophysics, Geosystems*, 17(2), 616–624. <https://doi.org/10.1002/2015gc006171>
- Bechtel, T. D., Forsyth, D. W., & Swain, C. J. (1987). Mechanisms of isostatic compensation in the vicinity of the East African Rift, Kenya. *Geophysical Journal International*, 90(2), 445–465. <https://doi.org/10.1111/j.1365-246X.1987.tb00734.x>
- Behn, M. D., Hirth, G., & Elsenbeck, J. R. (2009). Implications of grain size evolution on the seismic structure of the oceanic upper mantle. *Earth and Planetary Science Letters*, 282(1–4), 178–189. <https://doi.org/10.1016/j.epsl.2009.03.014>
- Brunsvik, B. R., Eilon, Z. C., & Lynner, C. (2021). Mantle structure and flow across the continent-ocean transition of the eastern north American margin: Anisotropic S-wave tomography. *Geochemistry, Geophysics, Geosystems*, 22(12). <https://doi.org/10.1029/2021GC010084>
- Eilon, Z. C., & Abers, G. A. (2017). High seismic attenuation at a mid-ocean ridge reveals the distribution of deep melt. *Science Advances*, 3(5), e1602829. <https://doi.org/10.1126/sciadv.1602829>
- Garcia, E. S., Sandwell, D. T., & Smith, W. H. F. (2014). Retracking CryoSat-2, Envisat and Jason-1 radar altimetry waveforms for improved gravity field recovery. *Geophysical Journal International*, 196(3), 1402–1422. <https://doi.org/10.1093/gji/ggt469>
- Hammond, W. C., & Humphreys, E. D. (2000). Upper mantle seismic wave velocity: Effects of realistic partial melt geometries. *Journal of Geophysical Research*, 105(B5), 10975–10986. <https://doi.org/10.1029/2000jb900041>
- Holtzman, B. K. (2016). Questions on the existence, persistence, and mechanical effects of a very small melt fraction in the asthenosphere. *Geochemistry, Geophysics, Geosystems*, 17(2), 470–484. <https://doi.org/10.1002/2015gc006102/pdf>
- Incorporated Research Institutions for Seismology. (2015). Data services products: Syngine. <https://doi.org/10.17611/DP/SYNGINE.1>
- Jackson, I., & Faul, U. H. (2010). Grain-size-sensitive viscoelastic relaxation in olivine: Towards a robust laboratory-based model for seismological application. *Physics of the Earth and Planetary Interiors*, 183(1–2), 151–163. <https://doi.org/10.1016/j.pepi.2010.09.005>
- Kennet, B., & Engdahl, E. R. (1991). Traveltimes for global earthquake location and phase identification. *Geophysics Journal International*, 105(2), 429–465. <https://doi.org/10.1111/j.1365-246x.1991.tb06724.x>
- Schmandt, B., & Humphreys, E. (2010). Seismic heterogeneity and small-scale convection in the southern California upper mantle. *Geochemistry, Geophysics, Geosystems*, 11(5), Q05004. <https://doi.org/10.1029/2010gc003042>
- Takei, Y., & Holtzman, B. K. (2009). Viscous constitutive relations of solid-liquid composites in terms of grain boundary contiguity: 1. Grain boundary diffusion control model. *Journal of Geophysical Research: Solid Earth and Planets*, 114(B6), B06205. <https://doi.org/10.1029/2008jb005850>
- Yamauchi, H., & Takei, Y. (2020). Application of a premelting model to the lithosphere-asthenosphere boundary. *Geochemistry, Geophysics, Geosystems*, 21(11). <https://doi.org/10.1029/2020GC009338>